ACS APPLIED MATERIALS & INTERFACES

www.acsami.org

Research Article

Multistep Sulfur Leaching for the Development of a Highly Efficient and Stable $NiS_x/Ni(OH)_2/NiOOH$ Electrocatalyst for Anion Exchange Membrane Water Electrolysis

Lu Xia, Wulyu Jiang, Heinrich Hartmann, Joachim Mayer, Werner Lehnert, and Meital Shviro*

Cite This: *ACS Appl. Mater. Interfaces* 2022, 14, 19397−19408

Read Online

ACCESS | Metrics & More | Article Recommendations | Supporting Information

ABSTRACT: Nickel (poly)sulfides have been widely studied as anodic catalysts for alkaline water electrolysis owing to their diverse morphologies, high catalytic activities in the oxygen evolution reaction (OER), and low cost. To utilize low-cost and high-efficiency polysulfides with industry-relevant cycling stability, we develop a Ni-rich $NiS_x/Ni(OH)_2/NiOOH$ catalyst derived from NiS_2/Ni_3S_4 nanocubes. Ni-rich $NiS_x/Ni(OH)_2/NiOOH$ shows improved OER catalytic activity (η = 374 mV@50 mA cm^{-2}) and stability (0.1% voltage increase) after 65 h of a galvanostatic test at 10 mA cm^{-2} compared with commercial Ni/NiO and hydrothermally synthesized $Ni(OH)_2$ (both show η > 460 mV@50 mA cm^{-2} along with 4.40 and 1.92% voltage increase, respectively). A water-splitting electrolyzer based on Pt/C||AF1-HNN8-50||$NiS_x/Ni(OH)_2/NiOOH$ exhibits a current density of 1800 mA cm^{-2} at 2.0 V and 500 h high-rate stability at 1000 mA cm^{-2} with negligible attenuation of only 0.12 mV h^{-1}. This work provides an understanding of truly stable species, intrinsic active phases of Ni polysulfides, their high-rate stability in a real cell, and sheds light on the development of stable chalcogenide-based anodic electrocatalysts for anion exchange membrane water electrolysis (AEMWE).

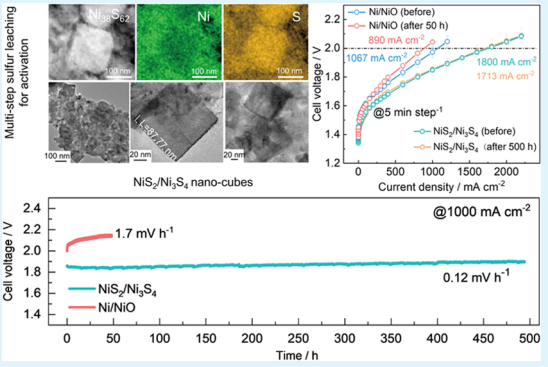

KEYWORDS: *nickle polysulfides, oxygen evolution reaction, alkaline water electrolysis, electrocatalysts, sulfur leaching*

1. INTRODUCTION

Water electrolysis is of great importance for mitigating the greenhouse gas effect and producing high-purity hydrogen.[1−7] However, proton exchange membrane water electrolysis (PEMWE) has been impeded by high stack cost and scarcity of platinum-group metal (PGM)-based catalysts,[2,8−11] while classic alkaline water electrolysis shows poor polarization performance due to low conductivity of porous diaphragms.[2] Therefore, an anion exchange membrane (AEM),[12−16] combined with non-PGM catalysts, has been proposed as a scalable and cost-effective route for large-scale applications, yet still hindered by poor stability and low operating current density.[17−20] In particular, the kinetically sluggish oxygen evolution reaction (OER) slows down the overall anion exchange membrane water electrolysis (AEMWE), as it involves four electrons and must first break O−H and then overcome the formation energy of the O−O bond.[21−25] Therefore, it is needed to develop highly active, stable, and low-cost PGM-free OER catalysts for AEMWE.

To date, tremendous efforts for OER catalysts have focused on oxides/hydroxides, chalcogenides, and pnictides based on transition metals on porous substrates such as nickel foam (NF), which have impressively low overpotentials.[24,26−37] For example, Kim et al. developed (i) graphene-nanoplatelets-supported NiFe-MOF,[34] (ii) ruthenium core−shell and Ni single atom-based Ni−Ru catalyst,[35] (iii) crystalline−amorphous Ni_2P@ $FePO_xH_y$, and (iv) amorphous NiFe (oxy)-hydroxides, all exhibiting a high OER performance of 170−220 mV@10 mA cm^{-2}.[36,37] Zhou et al. developed Ni_3S_2 nanorods on NF via a simple one-step hydrothermal process that exhibited 187 mV at 10 mA cm^{-2} in 0.1 M KOH.[38] However, Ni_3S_2/NF was only tested for 10 h at 10 mA cm^{-2} without supporting post-test development of the microstructure and composition. Additionally, Shang et al. fabricated the Ni_xS_y/NF catalyst by *in situ* growth, showing rapidly declined performance after only 1000 CVs.[39] Overall, *in situ*-grown catalysts on NF exhibit high activity (low overpotential) for OER, but have the following problems for single-cell tests of AEMWE: (i) unfulfillable repeatability (uneven distribution and uncontrollable mass loading), (ii) low stability underflow mode (without binder reinforcement, largely washed away), and (iii) complete microstructure destruction after tests.[30,31]

Received: January 21, 2022
Accepted: April 4, 2022
Published: April 22, 2022

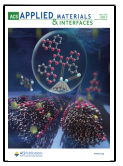

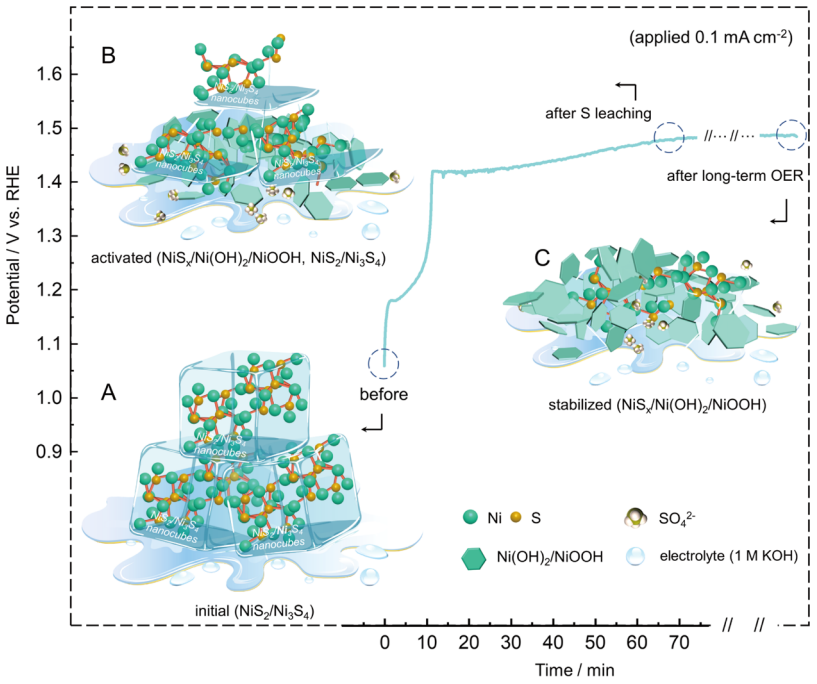

Figure 1. Schematic illustration of (A) NiS_2/Ni_3S_4 composite nanocubes as a "precatalyst" and corresponding (B) activated $NiS_x/Ni(OH)_2$/NiOOH covered with NiS_2/Ni_3S_4 residues and (C) fully stabilized $NiS_x/Ni(OH)_2$/NiOOH heterostructure.

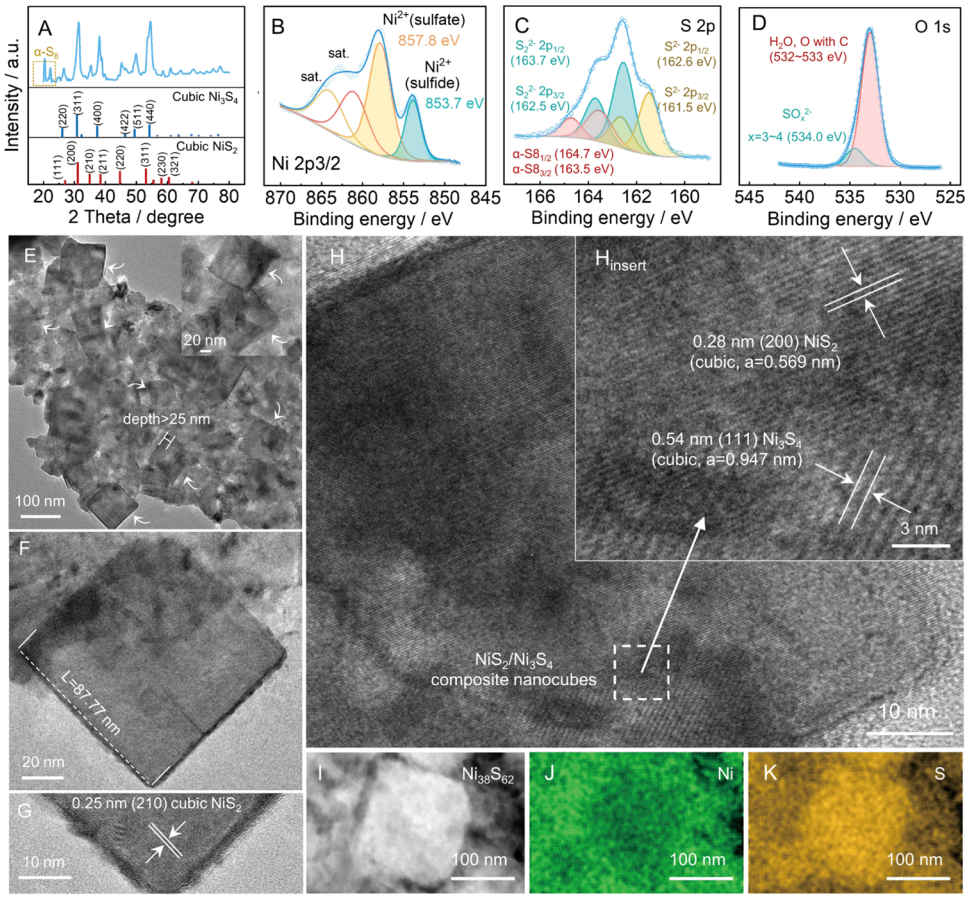

Figure 2. (A) XRD pattern of NiS_2/Ni_3S_4. (B) Ni 2p peaks and the fitting results, (C) S 2p peaks and the fitting results, and (D) O 1s peaks and the fitting results of the NiS_2/Ni_3S_4 catalyst. TEM, high-resolution TEM (HRTEM), HAADF-STEM images and corresponding elemental mappings of NiS_2/Ni_3S_4: (E) low-magnification TEM, (F) geometric size of single nanocube, (G) HRTEM images of the NiS_2 nanocube, (H) NiS_2/Ni_3S_4 composite nanocube, (I) HAADF-STEM image of NiS_2/Ni_3S_4 nanocube, and (J, K) distribution of Ni (green) and S (yellow) in EDX mappings.

https://doi.org/10.1021/acsami.2c01302
ACS Appl. Mater. Interfaces 2022, 14, 19397−19408

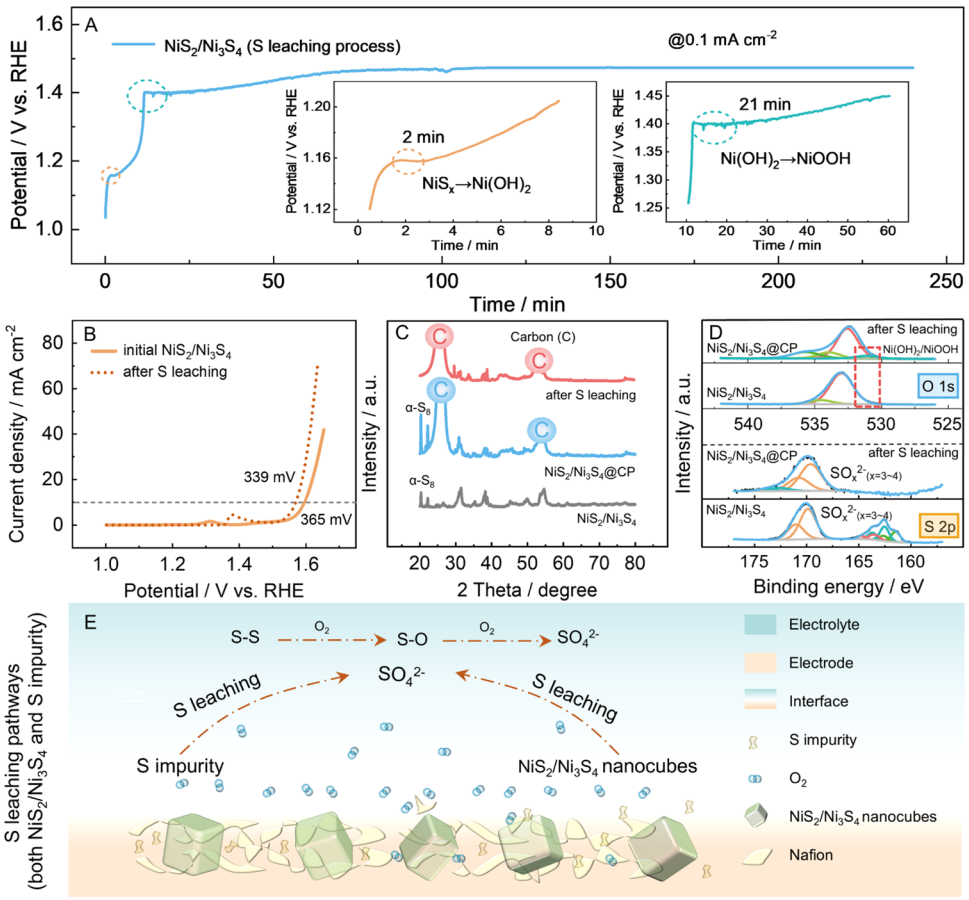

Figure 3. (A) Chronopotentiometry curve of NiS_2/Ni_3S_4 recorded at an ultralow current density of 0.1 mA cm^{-2} for the sulfur leaching process. (B) LSV curves of NiS_2/Ni_3S_4 before and after sulfur leaching in 1 M KOH recorded at 5 mV s^{-1}. (C, D) XRD patterns (C represents the peaks of the carbon substrate), XPS spectra of NiS_2/Ni_3S_4 after sulfur leaching. (E) Schematic illustration of sulfur leaching from NiS_2/Ni_3S_4 and the impurity.

Compared with uncontrollable self-supported structures, catalyst coating layers with more controllable ink dispersion and catalyst mass loading exhibit high reproducibility and stability due to binder strengthening.[17,40−43] However, metal (poly)sulfides are almost unstable under strong polarization in alkaline solution during OER processes, especially under an oxygen-filled atmosphere. It has been demonstrated that transition-metal chalcogenides (TMCs) would be irreversibly oxidized to corresponding oxides/(oxy)hydroxides (TMOs/TMHOs).[44−49] However, these studies have not yet pointed out the structural and morphological behaviors of (poly)-sulfides: (i) what extent (completely, partially) of sulfur leaching, (ii) the effect of residual sulfur on the stability of the (oxy)hydroxides, (iii) and more importantly, tangible high-current stability in single-cell tests, with almost no reports of polysulfides at a current density of ≥1000 mA cm^{-2}.

Here, we fabricated the NiS_2/Ni_3S_4 catalyst by a one-step, template-free method, the initial composition, phase, and microstructure of which were proved as S-rich NiS_2/Ni_3S_4 composite nanocubes (Figure 1A). Then, a multistep electrochemical leaching method was applied to leach sulfur from S-rich NiS_2/Ni_3S_4 nanocubes. NiS_2/Ni_3S_4 was first partially converted to $Ni(OH)_2$ (Figure 1B) and then to NiOOH, forming a highly stabilized Ni-rich $NiS_x/Ni(OH)_2$/NiOOH catalyst after long-term tests (Figure 1C). It exhibited higher activity and stability than commercial Ni/NiO and hydrothermally synthesized $Ni(OH)_2$ under both 100 mV s^{-1} cyclic voltammetry for 10 000 cycles and a constant current density of 10 mA cm^{-2} for 65 h. Moreover, this catalyst, coupled with Pt/C, was tested in single cells and exhibited higher performance (1800 mA cm^{-2} at 2.0 V) and higher stability (>500 h at 1000 mA cm^{-2}) than Ni/NiO (1067 mA cm^{-2}, <50 h) due to the refined and redistributed $NiS_x/Ni(OH)_2$/NiOOH structure, suppressing bubble-induced voltage increase and catalyst shedding.

2. RESULTS AND DISCUSSION

2.1. Structural Characterization. NiS_2/Ni_3S_4 was synthesized by a 4 h solvothermal method and explained in detail in Section 4. X-ray diffraction (XRD) was used to study the crystal structure of NiS_2/Ni_3S_4 (Figure 2A) and shows diffraction peaks at 2θ values corresponding to the planes of NiS_2 (JCPDS: 11-0099)[50−54] and Ni_3S_4 (JCPDS: 00-047-1739).[55,56] In addition, peaks of α-S_8 in a small angle range (20−25°) are attributed to the byproduct of thioacetamide (TAA, S precursor).[57] X-ray photoelectron spectroscopy (XPS) was used to investigate the surface chemical state of NiS_2/Ni_3S_4 (Figure 2B−D). The Ni 2p spectrum of NiS_2/Ni_3S_4 was fitted into two peaks at 857.8 and 853.7 eV corresponding to Ni^{2+} $2p_{3/2}$ (sulfate) and Ni^{2+} $2p_{3/2}$ (sulfide)-(Figure 2B),[50,52] indicating that pristine NiS_2/Ni_3S_4 almost fully consists of Ni^{2+}, which could result in low initial OER performance due to poor electrophilicity of adsorbed oxygen.[55,58,59] The S 2p spectrum (Figure 2C) was fitted into

https://doi.org/10.1021/acsami.2c01302
ACS Appl. Mater. Interfaces 2022, 14, 19397−19408

three peaks: the peaks at 161.5 and 162.6 eV correspond to $2p_{3/2}$ and $2p_{1/2}$ of S^{2-}.[50,52,53] The peaks at 162.5 and 163.7 eV are attributed to $2p_{3/2}$ and $2p_{1/2}$ of S_2^{2-}.[51,52,60] Moreover, the peaks at 163.5 and 164.7 eV are assigned to the spin−orbit of $2p_{3/2}$ and $2p_{1/2}$ in α-S_8, indicating the remnants of S from TAA during the sulfurization process, which was produced by the reaction between S_n^{2-} and H^+ due to decreased pH.[50,61] The binding energies of O 1s at ∼529 and ∼531 eV, corresponding to NiO and $Ni(OH)_2$, were not detected (Figure 2D),[62,63] indicating no oxides and hydroxides on the surface of the pristine NiS_2/Ni_3S_4 catalyst. Therefore, the surface of NiS_2/Ni_3S_4 is mainly composed of Ni^{2+}, S^{2-}, and S_2^{2-}.

The morphology of NiS_2/Ni_3S_4 was observed by transmission electron microscopy (TEM). Figure 2E−G shows that NiS_2/Ni_3S_4 inherits the cube-shaped morphology with a size of 80 ± 20 nm and the thickness of the nanocube is greater than 25 nm. This is achieved by moderate pH for producing elemental sulfur that would further react with nickel sulfides to form NiS_2/Ni_3S_4 polysulfides (Figure S1) and can be controlled by the reaction time. Sulfur species suffered from precipitation with Ni^{2+} (after 2 h of reaction, leading to the formation of NiS/Ni_3S_4), polymerization with elemental S to form polysulfides (after 4 h, leading to the formation of NiS_2/Ni_3S_4), and their dissolution (after 6 h, leading to the formation of NiS/NiS_2) with the release of H_2S gas.[61] Figure 2H shows the high-resolution TEM image with lattice fringes with an interplanar spacing of 0.28 and 0.54 nm, corresponding to the (200) lattice planes of NiS_2 and the (111) lattice planes of Ni_3S_4, further confirming the crystal structures of NiS_2 and Ni_3S_4 shown by XRD measurements.[51,64] The high-angle annular dark-field scanning transmission electron microscopy (HAADF-STEM) image and the corresponding energy-dispersive X-ray (EDX) mapping of NiS_2/Ni_3S_4 shows the distribution of Ni and S throughout the composite structure (Figure 2I−K). Furthermore, it is worth noting that the quantitative EDX analysis ($Ni_{38}S_{62}$) is consistent with the XPS and XRD results analyzed above.

2.2. Electrochemically Assisted Sulfur Leaching. The electrocatalytic behaviors of NiS_2/Ni_3S_4 were investigated for the OER in 1 mol L^{-1} KOH on a glassy carbon electrode or carbon paper (CP). Surface reconstruction of the polysulfides takes place in a highly polarized oxidation environment and sulfur could be leached out into the electrolyte. The (oxy)hydroxide/polysulfide catalyst formed by the *in situ* electrochemical tests (while sulfur was leached out) exhibited higher electrochemical performance than their "initial form" and the hydrothermally synthesized oxides/hydroxides.[45−47] Therefore, before recording linear sweep voltammetry (LSV), the focus was on studying the sulfur leaching process at an ultralow current density of 0.1 mA cm^{-2} (Figure 3A). Two platforms were observed during sulfur leaching: at 1.160 V for 2 min and 1.400 V for 21 min, indicating structural evolution from initial NiS_2/Ni_3S_4 to NiOOH *via* $Ni(OH)_2$ as an intermediate species.[49] As shown in Figure 3B, the suppression of overpotential from 365 (initial NiS_2/Ni_3S_4) to 339 mV leads to a 7.12% reduction. After sulfur leaching, only the oxidation peak of $Ni(OH)_2$ remains at 1.381 V, indicating that surface sulfur in S-rich NiS_x was leached out and exhibits no oxidation peaks at 1.313 V. To support this observation, XPS, XRD, Fourier transform infrared (FTIR) spectrometer, and STEM-EDX were used to investigate the structure after sulfur leaching. XRD results (Figure 3C) show that the sulfur impurity peaks at 20−25° and the peaks of NiS_2/Ni_3S_4 at 35.3 and 45.3° disappeared, indicating phase transformation of polysulfides. In addition, FTIR of NiS_2/Ni_3S_4 after electrochemical oxidation at 1.35 V for 6 h exhibits an emerged peak at 3640 cm^{-1}, attributed to nonhydrogen bonded hydroxide (OH^-) in $Ni(OH)_2$, while the peaks around 800−1000 cm^{-1} for NiS_x (NiS_2, Ni_3S_4) are weakened, indicating that NiS_2/Ni_3S_4 was partially transformed to $Ni(OH)_2$ at the first oxidation stage (∼1.3 V).[65] Meanwhile, FTIR spectrometry of NiS_2/Ni_3S_4 (Figure S4A) shows an attenuated peak at 3640 cm^{-1} after 6 h at 1.70 V, which agrees well with the result from Yavuz et al. who held $Ni(OH)_2$ under different voltages and concluded that the decreased peak intensity of $Ni(OH)_2$ was due to its oxidation to NiOOH at 1.4−1.5 V.[66] To detect the product of S leaching in the electrolyte, the anions in the electrolyte were precipitated by barium (Ba^{2+}) ions after the electrochemical test and excluded by hydrochloric and nitric acids for carbonate (CO_3^{2-}) and then further analyzed by FTIR. The peaks are largely identical to those of the reported barium sulfate (Figure S4B).[67] The XPS results after the sulfur leaching process support this observation with the disappeared peaks at 160−165 eV in the S 2p region (Figure 3D) and the emerged peak at ∼531.0 eV in the O 1s region of NiS_2/Ni_3S_4, indicating sulfur leaching and the formation of nickel(oxy)-hydroxide. In addition, the HAADF images, as well as the corresponding elemental mappings present higher atomic ratios for nickel in the structure and lower ones for sulfur: $Ni_{93}S_7$ (Figure S4C−E), further supporting the leaching of sulfur from NiS_2/Ni_3S_4. Two possible pathways of sulfur leaching have been proposed and presented in Figure 3E. The S−S bond in the α-S_8 impurity (XRD, Figure 3C) can be oxidized to the S−O bond and then to sulfate ions that are soluble in the electrolyte, as shown in the XPS results (Figure 3D, S 2p, ∼169.0 eV). The sulfur in NiS_2/Ni_3S_4 can be oxidized to the S_x impurity (S−S), and then follow the leaching path of the S−S bond to sulfate ions.

The activity enhancement of NiS_2/Ni_3S_4 obtained by the reaction time of 4 h after sulfur leaching prompted us to investigate whether further improvement in activity was possible when changing the reaction time to 2 or 6 h. The Ni−S-2 h and Ni−S-6 h show an increase in performance after sulfur leaching but are less active than the 4 h reaction (Figure S2). These differences in performance can be explained by both morphologies and phase compositions. The TEM and HRTEM images show that Ni−S-2 h consisted of nanoparticles with a size of 20 ± 5 nm, whereas large aggregates were observed for Ni−S-6 h (Figure S3). Moreover, the phase composition of the catalysts changed with the reaction time: for Ni−S-2 h, the hexagonal NiS (JCPDS: 75-0613)[54] and a small number of cubic NiS_2 (JCPDS: 1-0099)[50−54] and Ni_3S_4 (JCPDS: 00-047-1739) were detected (Figure S5). For Ni−S-6 h, there was a mixture of α-S_8 and $NiS/NiS_2/Ni_3S_4$. These results agree well with the literature, which explains that after the initial coprecipitation of Ni^{2+} and S^{2-} (2 h), more complicated S-rich polysulfides were formed with longer vulcanization time (4 h), and then some super-rich polysulfides were dissolved in low pH solutions (6 h).[61] Therefore, NiS_2/Ni_3S_4, which consists of more conductive and active polysulfides with the microstructure of small-sized nanocubes, shows better OER performance than Ni−S-2 h with more NiS phase, and Ni−S-6 h with the NiS phase and large particle size.

2.3. Half-Cell Performance. To further evaluate the activity of the designed NiS_2/Ni_3S_4, the OER performance compared with commercial Ni/NiO is presented in Figure

https://doi.org/10.1021/acsami.2c01302
ACS Appl. Mater. Interfaces 2022, 14, 19397−19408

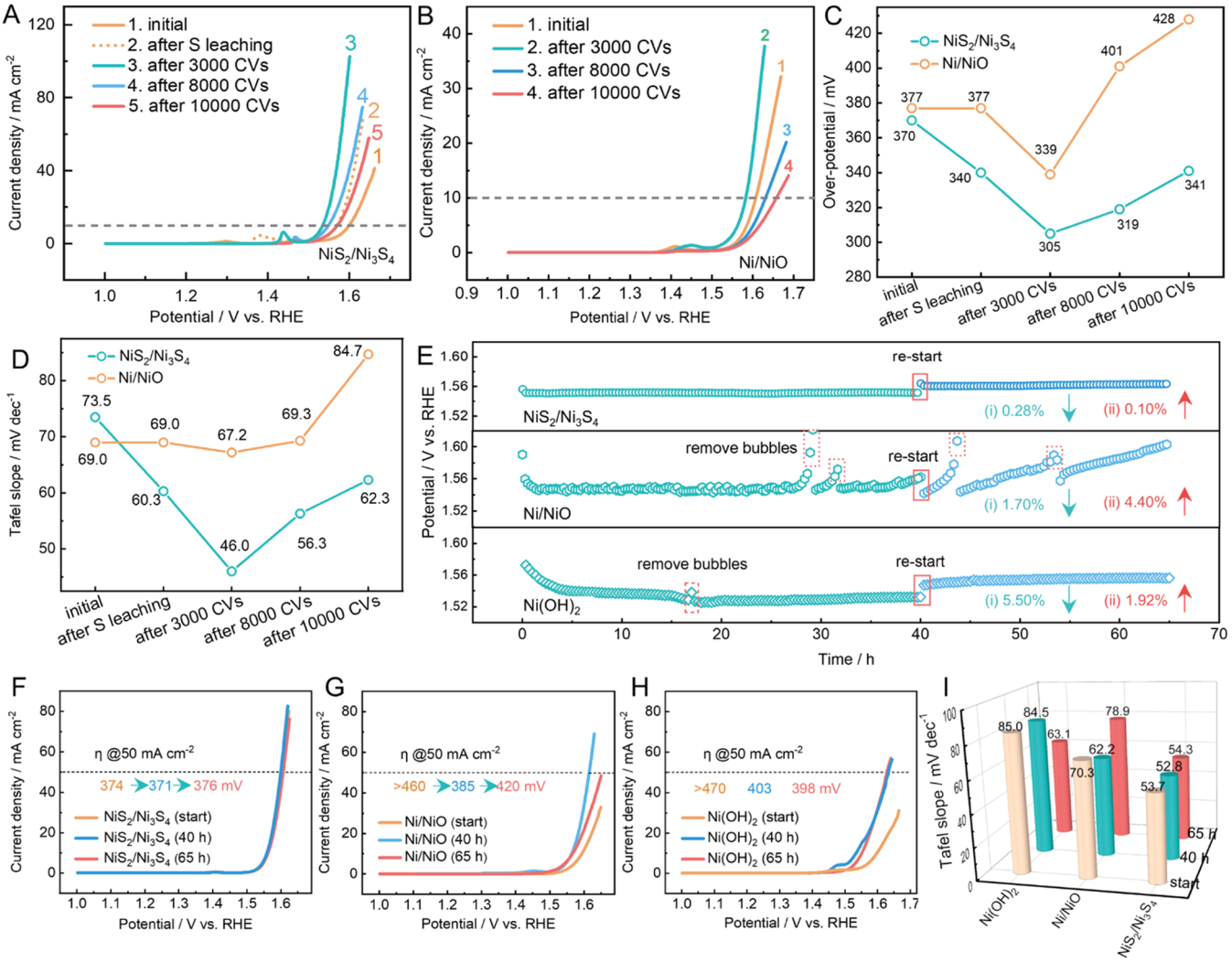

Figure 4. (A, B) LSV curves recorded at 5 mV s^{-1} and (C, D) corresponding overpotential at 10 mA cm^{-2} and Tafel slopes of NiS_2/Ni_3S_4 and commercial Ni/NiO before and after sulfur leaching, 3000, 8000, and 10 000 CVs in 1 M KOH. (E) OER stability of NiS_2/Ni_3S_4 after sulfur leaching, Ni/NiO and $Ni(OH)_2$ at a constant current density of 10 mA cm^{-2}. (F) LSV curves of NiS_2/Ni_3S_4 after sulfur leaching, 40 and 65 h, (G) Ni/NiO and (H) $Ni(OH)_2$ before and after 40 and 65 h in 1 M KOH recorded at 5 mV s^{-1}, and (I) corresponding Tafel slopes of NiS_2/Ni_3S_4, $Ni(OH)_2$, and Ni/NiO.

4A,B. The corresponding onset potentials and overpotentials at 10 mA cm^{-2} (η_{10}) are summarized in Table S1 and Figure 4C. Initially, the onset potential of NiS_2/Ni_3S_4 (1.554 V) resembled that of Ni/NiO (1.529 V) but improved after sulfur leaching (1.492 V). After 3000 CV cycles, onset potentials of NiS_2/Ni_3S_4 and Ni/NiO decrease to 1.478 and 1.497 V, respectively. Increasing the number of cycles to 8000 and 10 000, we found that the catalytic stability of NiS_2/Ni_3S_4 is superior to that of commercial Ni/NiO with a lower onset potential increase of only 0.021 V (0.031 V for Ni/NiO) from 3000 to 10 000 CVs. Moreover, the η_{10} of NiS_2/Ni_3S_4 changes from 370 mV (initial) to 305 mV after 3000 CVs and to 341 mV after 10 000 CVs, while for Ni/NiO the trend is from 377 mV (initial) to 339 mV (after 3000 CVs) and 428 mV (after 10 000 CVs). The difference lies in an extra improvement of OER catalytic activity for NiS_2/Ni_3S_4 from initial to that after sulfur leaching, owing to the formation of more active $NiS_x/Ni(OH)_2$/NiOOH heterostructure and the electrochemical tuning effect during the pretreatment process.[45,48,68−70] The electrochemically active surface area was calculated and shows that the double-layer capacitance (C_{dl}) value of NiS_2/Ni_3S_4 is 0.422/0.451 mF cm^{-2} (initially/after sulfur leaching), which is almost as double as that of Ni/NiO for 0.235 mF cm^{-2} (Figure S6), indicating that NiS_2/Ni_3S_4 has a larger ECSA and exposes more active sites and thus performs better. Electrochemical impedance spectroscopy (EIS) was further employed to evaluate the charge transfer process of catalysts. The charge transfer resistance (R_{ct}) of the initial NiS_2/Ni_3S_4 is higher than that of Ni/NiO and $Ni(OH)_2$ due to the sulfur impurity (Figure S7). After sulfur leaching, the R_{ct} of NiS_2/Ni_3S_4 decreases and becomes lower than that of Ni/NiO and $Ni(OH)_2$. This indicates Ni-rich $NiS_x/Ni(OH)_2$/NiOOH produced by sulfur leaching can improve the charge transfer efficiency of pristine NiS_2/Ni_3S_4. As can be concluded from XPS, XRD, ECSA, and EIS results, the Ni-rich $NiS_x/Ni(OH)_2$/NiOOH are more active and conductive than pristine NiS_2/Ni_3S_4.

Tafel plots of NiS_2/Ni_3S_4 and Ni/NiO are summarized in Figure 4D and show a similar tendency as η_{10}: from 73.5 (initial), 46.0 (after 3000 CVs) to 62.3 mV dec^{-1} (after 10 000 CVs) for NiS_2/Ni_3S_4 and from 69.0 (initial), 67.2 (after 3000 CVs) to 84.7 mV dec^{-1} (after 10 000 CVs) for Ni/NiO.

https://doi.org/10.1021/acsami.2c01302
ACS Appl. Mater. Interfaces 2022, 14, 19397−19408

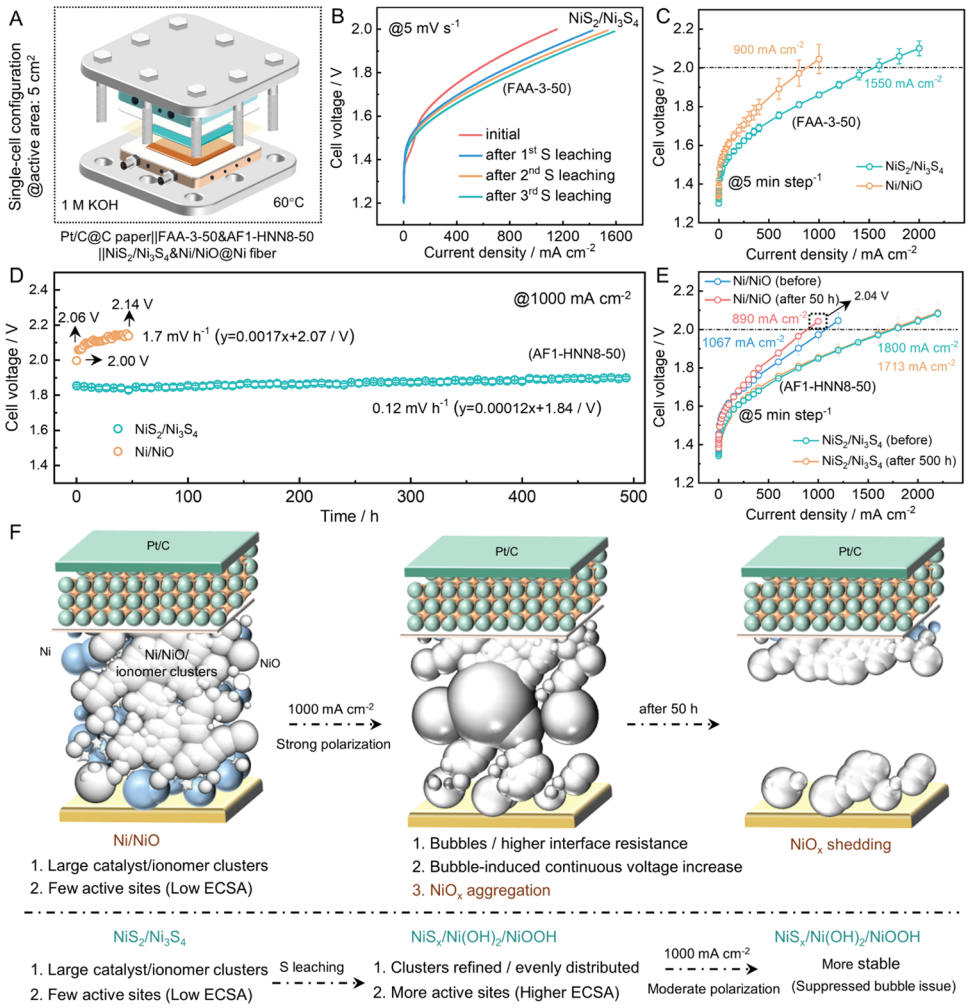

Figure 5. (A). Illustration of the single-cell configuration. (B) Polarization curves of the cell, Pt/C||FAA-3-50||NiS_2/Ni_3S_4, before and after three times of sulfur leaching by a dynamic potential scanning method at 5 mV s^{-1}. (C) Polarization curves after conditioning at 1.7 V for 6 h by a galvanostatic method (5 min $step^{-1}$), (D) stability at 1000 mA cm^{-2}, (E) polarization curves before and after stability tests, and (F) degradation and stability analysis of Ni/NiO- and NiS_2/Ni_3S_4-based cells.

Furthermore, there is an additional enhancement in the catalytic kinetics for NiS_2/Ni_3S_4 from initial to post sulfur leaching due to instantaneous oxidation of the surface nickel sulfides to hydroxides, forming a hybrid structure of NiS_x/$Ni(OH)_2$/NiOOH. Looking more closely at a long-term test from 3000 CV cycles to 10 000 CV cycles, the deterioration in performance with increasing overpotential could be explained by three possible reasons:

(1) Continued sulfur leaching and phase transformation: as confirmed by the XRD, the peak shifts occur but are not fully consistent with the specific phase due to the partially amorphous structure after electrochemical oxidation (Figure S9).[63] Moreover, the XPS supports the formation of more $Ni(OH)_2$/NiOOH species on the surface during the cycling process (Figure S10B), while SEM-EDX mapping of the electrodes confirms that sulfur was continuously leached to a large extent, from "initial (0%)", "after S leaching (66.7%)", "after 3000 CVs (80.6%)", to "after 10 000 CVs (96.6%)" (Figure S10C), suggesting that ca. 20 wt % sulfur within the catalyst surface best promotes OER activity.

(2) Microstructure changes: the microstructure changed with different cycles of cyclic voltammetry, which can be supported by HAADF images and corresponding elemental mappings after 3000 (Figure S11) and 10 000 CVs (Figure S12). Finally, NiS_2/Ni_3S_4 was transformed into nanoparticles.

(3) Catalyst shedding: part of NiS_2/Ni_3S_4 fell off into the electrolyte and caused a direct decrease in catalytic activity, which can be inferred from weakened peaks of S 2p (Organic S from Nafion, 170−175 eV, Figure S10A).

In addition to the excellent electrocatalytic activity, the NiS_2/Ni_3S_4 electrocatalyst also shows remarkable stability with a potential increase of only 11.0 mV after 65 h at 10 mA cm^{-2} (Figure 4E). In comparison, 59.9 and 23.8 mV potential increase has been recorded for Ni/NiO and $Ni(OH)_2$, respectively. LSV curves before and after 40 and 65 h are shown in Figure 4F−H. First, η_{50} of NiS_2/Ni_3S_4 increases by only ~2 mV (~0.53%) before and after 65 h, with an average η_{50} of 373.7 mV. However, the current density of Ni/NiO and $Ni(OH)_2$ cannot reach 50 mA cm^{-2} at the beginning, and the η_{50} of Ni/NiO increases by ~35 mV (~9.09%) from "after 40 h" to "after 65 h", with an average value of 402.5 mV, while with an average value of 400.5 mV for $Ni(OH)_2$, indicating the best activity and stability of NiS_2/Ni_3S_4.

https://doi.org/10.1021/acsami.2c01302
ACS Appl. Mater. Interfaces 2022, 14, 19397−19408

Tafel slopes (Figure 4I, supported by Figure S13) show that NiS_2/Ni_3S_4 almost kept at an average value of 53.6 mV dec^{-1}, which is much lower and stable than that of Ni/NiO and $Ni(OH)_2$ at average values of 70.5 and 77.5 mV dec^{-1}, indicating faster and stable kinetics. The active sites of NiS_2/Ni_3S_4, Ni/NiO, and $Ni(OH)_2$ are mainly the Ni in NiOOH,[49,63] but the difference lies in the surface morphology and phase composition. With Ni-rich polysulfide, NiS_2/Ni_3S_4 after long-term tests exhibits better stability and performance retention, which is promising as an anodic catalyst in AEMWE single cells.

Recently, the performance improvement of Ni-based catalysts after electrochemical tests was attributed to iron impurities.[71,72] In this sense, the OER performance of NiS_2/Ni_3S_4 in 1 M NaOH was also studied and compared with 1 M KOH (Figure S8), and the corresponding overpotentials (η_{10}) are summarized in Table S2. The NiS_2/Ni_3S_4 catalyst in KOH and NaOH shows almost the same results after sulfur leaching (341 mV in NaOH, 340 mV in KOH) and after 3000 CVs (311 mV in NaOH, 305 mV in KOH), suggesting that the performance improvement is not related to Fe impurities in the electrolyte solution but sulfur leaching and phase transformation effects.

2.4. Single-Cell Performance. Inspired by the electrocatalytic activity and stability of NiS_2/Ni_3S_4 toward OER, an alkaline electrolyzer was constructed to investigate its feasibility for practical water splitting. The adopted single-cell configuration is shown in Figure 5A and is as follows: End plate||current collector, electrolyte channel, and heater||PTFE||Pt/C@C paper||FAA-3-50||Ni−S or Ni/NiO. Two representative cells based on Ni/NiO and NiS_2/Ni_3S_4 and a detailed test protocol are presented in Figures S14 and 15. To be consistent with the half-cell tests, the stabilization process of sulfur leaching (Figure S16A) was also maintained in the single-cell tests with the same potential scan rate of 100 mV s^{-1}. After three times of sulfur leaching, the current density of the NiS_2/Ni_3S_4-based cell (Figure 5B) increases from 1152 mA cm^{-2} (initial) to 1424 mA cm^{-2} (1st), 1539 mA cm^{-2} (2nd), and 1587 mA cm^{-2} (3rd) at 2.0 V. This suggests that the leaching of sulfur from S-rich to Ni-rich NiS_x with the formation of a $NiS_x/Ni(OH)_2/NiOOH$ heterostructure contributes to the improvement of cell performance, which is consistent with the results from the half-cell test. To provide a fair comparison, Ni/NiO-based cells also underwent the sulfur leaching process (Figure S16B). After sulfur leaching three times, the current density of Ni/NiO-based cells remains stable with specific values ranging from 1417 mA cm^{-2} (initial) to 1419 mA cm^{-2} (1st), 1421 mA cm^{-2} (2nd), and 1414 mA cm^{-2} (3rd) at 2.0 V (Figure S17A,B), indicating that sulfur leaching is the crucial factor for the performance improvement of NiS_2/Ni_3S_4-based cells. Moreover, the EIS results of both cells (Figure S18) are similar to those of the half-cell tests (Figure S7), suggesting that sulfur leaching causes a drop in internal resistance (R_Ω) and R_{ct}.

After 2 h of system temperature stabilization and 0.5 h of open-circuit voltage, both Ni/NiO- and NiS_2/Ni_3S_4-based cells were held at 1.7 V for 6 h for further conditioning. The current density of the Ni/NiO-based cell continuously decreases from 400 to 336 mA cm^{-2}, while the current density of the NiS_2/Ni_3S_4-based cell remains stable at 445 mA cm^{-2}, except for a slight decrease in the first 0.5 h from 469 to 445 mA cm^{-2}, while the current density (Figure S19A, 5 mV s^{-1}) increases from 1587 (after the 3rd sulfur leaching) to 1738 mA cm^{-2} (after conditioning), indicating better stability under moderate polarization conditions and further S-leaching-induced performance improvement of the NiS_2/Ni_3S_4-based cell. Meanwhile, the faradic efficiency of the initial cell (92.2% to 94.8%) is much lower than that after conditioning at 1.7 V for 6 h (97.4%), indicating that a small amount of current was used to oxidize sulfur to sulfate ions (Figure S19B,C). After conditioning, polarization performance was tested using a galvanostatic method, which is more accurate than dynamic scanning. As shown in Figure 5C, the NiS_2/Ni_3S_4-based cell exhibits a much higher current density of 1550 mA cm^{-2} than the Ni/NiO-based cell with only 900 mA cm^{-2} and most FAA-3-50-based cells in the literature (Table S3), indicating that NiS_2/Ni_3S_4 can also be activated for higher catalytic activity than Ni/NiO in full cells.

To verify the stability of NiS_2/Ni_3S_4 under continuous operation, a more stable membrane "AF1-HNN8-50" was used as the ionic conductor. As shown in Figure 5E, NiS_2/Ni_3S_4-based cells assembled with AF1-HNN8-50 membranes exhibit a further improved current density of 1800 mA cm^{-2} at 2.0 V, which is also much higher than that of Ni/NiO-based cells showing 1067 mA cm^{-2}. Then, the long-term test (Figure 5D) shows that NiS_2/Ni_3S_4-based cells are highly stable with a low voltage increase rate of 0.12 mV h^{-1}, while that of Ni/NiO-based cells is as high as 1.7 mV h^{-1}. Compared with the reported single-cell stability (Figure S20A−C and Table S4), the cells based on Pt/C||AF1-HNN8-50||NiS_2/Ni_3S_4 exhibit one of the lowest "voltage increase rates" under the highest current density of 1000 mA cm^{-2} for a long duration of 500 h. The current density at 2.0 V (Figure S21A,B) decreases from 1800 mA cm^{-2} (initial), 1600 mA cm^{-2} (after 185 h), 1512 mA cm^{-2} (after 310 h), and 1455 mA cm^{-2} (after 400 h) to 1400 mA cm^{-2} (after 500 h), while that of Ni/NiO-based cells decreased from 1067 to 890 mA cm^{-2} after only 50 h. The EIS shows that the degradation is not caused by the R_{ct} of the electrodes but by the continuous increase of the membrane resistance, as evidenced by the constant semicircle diameter and a slight right shift in EIS curves (Figure S21C) at 1000 mA cm^{-2} (membrane-resistance-controlled stage, which increases gradually). On the other hand, the degradation of the Ni/NiO-based cells after 50 h is due to an increased R_{ct}, while the membrane resistance remains unchanged (Figure S21D). After opening the cells, it was found that NiS_2/Ni_3S_4 remained on the substrates, and the membrane was brittle due to the high pressure, temperature, and current density (Figure S22A), while Ni/NiO was washed out entirely (Figure S22B). After membrane refreshing (all other conditions remained unchanged), the first intercept with the X-axis and the size of the semicircle in the EIS (Figure S22C) were found to be highly consistent with the initial condition, indicating a restored membrane-dominated internal resistance and a nearly unchanged R_{ct}. After that, the polarization curves after 500 h were retested and compared with the initial curve in Figure 5E. The current density of NiS_2/Ni_3S_4-based cells at 2.0 V remains stable from 1800 to 1713 mA cm^{-2} with a high retention rate of 95.2%, indicating that the catalyst is still active and promising for longer-term performance, and only hindered by membrane stability. The current density of Ni/NiO-based cells decreases from 1067 to 890 mA cm^{-2}, exhibiting much lower performance retention. As shown in Figure 5F, the high stability of NiS_2/Ni_3S_4-based cells can be attributed to suppressed bubble issues due to the refined and redistributed $NiS_x/Ni(OH)_2/NiOOH$ structure with a higher surface area,

https://doi.org/10.1021/acsami.2c01302
ACS Appl. Mater. Interfaces 2022, 14, 19397−19408

supported by the SEM images before and after 500 h. The surface morphology of the initial NiS_2/Ni_3S_4@nickel fiber consists of large catalyst/ionomer clusters with a diameter of 1−5 μm (Figure S23A,C), while after 500 h the surface morphology is mainly composed of $NiS_x/Ni(OH)_2$/NiOOH-based nanosheets with the diameter of 300−500 nm (Figure S23B,D).

Meanwhile, Ni/NiO-based cells suffered from serious bubble issues (also in RDE tests, Figure 4E), with the cell voltage increasing from 2.00 to 2.14 V (Figure 5D), while it is only 2.04 V in the polarization curve after 50 h at 1000 mA cm^{-2} (Figure 5E). This indicates a reversible voltage increase of 0.1 V caused by bubbles, which would increase the interfacial resistance in the long term and lead to a continuous voltage increase, promoting catalyst aggregation, shedding, and printing onto the membrane (Figure S22B).

3. CONCLUSIONS

A highly stabilized Ni-rich $NiS_x/Ni(OH)_2$/NiOOH heterostructure was electrochemically derived from S-rich NiS_2/Ni_3S_4 composite nanocubes by a multistep sulfur leaching process, with higher ECSA and conductivity than commercial Ni/NiO and hydrothermally synthesized $Ni(OH)_2$. The morphological, structural, and compositional behaviors of Ni (poly) sulfides before and after OER processes were clarified by STEM, XRD, and XPS. It was proved that the initial S-rich NiS_2/Ni_3S_4 composite nanocubes would be converted to Ni-rich NiS_x and $Ni(OH)_2$/NiOOH that exhibited higher ECSA and conductivity after sulfur leaching, acting as true intrinsic species for OER. Meanwhile, polysulfides exhibited better electrochemical behaviors during 10 000 CVs at 100 mV s^{-1} than commercial Ni/NiO and hydrothermally synthesized $Ni(OH)_2$. More importantly, the $NiS_x/Ni(OH)_2$/NiOOH catalyst exhibited stable thermodynamic (overpotential) and kinetic (Tafel slope) performance during 65 h@10 mA cm^{-2} in a half-cell and 500 h@1000 mA cm^{-2} in a flow-mode full cell with negligible degradation, which can be practically applicable as an anodic catalyst for AEMWE. The present work provides a fundamental understanding and a specific approach to better utilize S-rich Ni (poly)sulfides and promotes further development of AEMWE by highly stabilized, Ni-rich, and low-cost anodic electrocatalysts.

4. EXPERIMENTAL SECTION

4.1. Materials. Chemicals and materials: Nickel chloride ($NiCl_2$), thioacetamide (C_2H_5NS), and sodium hydroxide (NaOH) were purchased from Sigma-Aldrich and used without further purification. Potassium hydroxide (KOH) was purchased from Merck KGaA (EMSURE). Ni/NiO nanopowder was purchased from Alfa-Aesar. Carbon paper and Ni fiber were purchased from Toray and Bekeart, respectively. FAA-3-50 and AF1-HNN8-50 membranes, and FAA-3-SOLUT-10 and AP1-HNN8-00-X ionomers were supplied by Fumatech and Ionomr Innovations Inc. (Aemion), respectively.

4.2. Ni−S Catalyst Synthesis. $NiCl_2$ (3.5 mmol) was dissolved in 60 mL of deionized (DI) water and then mixed with 1 mL of KOH solution (10 mM) under vigorous stirring for 5 min. Thioacetamide was then added slowly with vigorous stirring for 30 min. The mixture was further stirred and kept at 160 ± 2 °C for 2, 4, and 6 h (Figure S1). During this period, evaporated water from the flask was renewed every 30 min. The resulting black precipitates denoted as Ni−S-2 h, Ni−S-4 h, and Ni−S-6 h were filtrated and washed with deionized (D.I.) water and ethanol several times until a clear supernatant was observed. All precipitates were dried in a vacuum oven at room temperature for 24 h.

4.3. $Ni(OH)_2$ Catalyst Synthesis. $Ni(OH)_2$ was prepared by direct precipitation of 3.5 mM $NiCl_2$ and 7.0 mM KOH under strong stirring for 4 h at 160 ± 2 °C. Washing and separation processes were the same as that of Ni−S catalysts.

4.4. Characterization Studies. The crystal information of Ni−S catalysts was studied by X-ray powder diffraction (D8 DISCOVER, Bruker) with a Cu K_α target. The morphology, elemental distribution, and detailed structural information were studied by scanning transmission electron microscopy (STEM), and energy-dispersive X-ray (EDX) spectroscopy on a Titan 80-200 electron microscope (Thermo Fisher Scientific) with a probe corrector (CEOS) and a high-angle annular dark-field (HAADF) detector, and high-resolution transmission electron microscopy (HRTEM) on a Titan 80-300 electron microscope (Thermo Fisher Scientific).[73,74] The chemical valence states of Ni−S samples were studied by X-ray photoelectron spectroscopy (XPS, PhiS000 VersaProbeII, ULVAC-Phi Inc) with Al Kα as the monochromatic (1.486 keV) source.[10] The catalysts for XRD and XPS were coated on the carbon paper (ca. 2.0 mg cm^{-2}) by the drop-by-drop method with the same ink for RDE. After electrochemical measurements, the catalyst was removed by ultrasonic separation from RDE for TEM/HRTEM/STEM. The detection of structural changes in NiS_2/Ni_3S_4 before and after electrochemical tests, and the proof of sulfate ions in the electrolyte were achieved by Fourier transform infrared spectrometry (FTIR, Monolithic diamond GladiATR, PIKE Technologies). The samples were prepared as follows: (i) the NiS_2/Ni_3S_4 catalyst was deposited on a graphite substrate with Nafion as a binder; (ii) two of the above electrodes were used as working electrodes and kept at 1.35 and 1.7 V for 6 h, respectively; (iii) the catalyst on the electrodes was scraped off after the OER tests and cleaned with ethanol and D.I. water. Analysis steps for sulfate ions in the electrolyte after electrochemical tests were conducted as follows: First, a NiS_2/Ni_3S_4-coated nickel fiber with an area of 10 cm^2 and mass loading of 20 mg cm^{-2} was used as the working electrode and kept at 1.7 V for 1 h in 150 mL of 1 M KOH. Then, excessive barium chloride ($BaCl_2$) was added into the above electrolyte and the pH of the mixture was further adjusted to "strong acid pH (< 1)" using hydrochloric acid to remove $BaCO_3$, etc. And then, the resulting precipitate was collected and washed repeatedly with dilute nitric acid three times to further remove other acid-soluble precipitates. After the above steps, the obtained white particles were only to be $BaSO_4$ or AgCl. Finally, fully dried powder was analyzed by FTIR.

4.5. Electrochemical Measurements. A glassy carbon (GC) electrode with a geometric area of ca. 0.19625 cm^2 was polished with an Al_2O_3 slurry. Eight milligrams of catalyst powder was dispersed with 0.5 mL of DI water, 1.5 mL of IPA, and 20 μL of 5 wt % Nafion solution to form a homogeneous ink suspension. Ink suspension (10 μL) was dropped onto the GC electrode with a mass loading of 0.2 mg cm^{-2}. A rotating disk electrode (RDE, Pine Research Instrumentation) system with an electrochemical workstation (VSP-150, BioLogic Sciences Instruments) was used for the electrochemical tests. The three-electrode system was composed of the electrolyte (200 mL of 1 M KOH), working electrode (catalyst-coated GC), counter electrode (platinum wire), and reference electrode (Hg/HgO). The obtained potential was corrected by the gap between Hg/HgO and RHE (0.926 V) and 85% of the internal resistance (IR) loss compensation according to the equation: $E_{iR\text{-corrected}} = E + 0.926 - 0.85 \times iR_s$ (where R_s represents the solution resistance tested by high-frequency AC impedance from 1 to 10^6 Hz with an amplitude of 0.005 V).[75] OER catalytic activity was checked by the linear sweep voltammetry (LSV) method. For the results "before sulfur leaching", Ni−S catalysts were directly tested by LSV (1.0−1.7 V, 5 mV s^{-1}) without any pretreatment under oxygen-saturated conditions. For the results "after sulfur leaching", the cyclic voltammetry (CV) method (1.0−1.7 V, 100 mV s^{-1}) was utilized to activate Ni−S by sulfur leaching: 10 cycles first and LSV were compared with that of "before sulfur leaching", and then the electrolyte was refreshed. After that, 3−4 times 10-cycle CV pretreatment was repeated until there was no obvious change of LSV curves. For the results "after CVs", the conditions (1.0−1.7 V, 100 mV s^{-1}) were the same as those of "CVs

https://doi.org/10.1021/acsami.2c01302
ACS Appl. Mater. Interfaces 2022, 14, 19397−19408

pretreatment". For Ni/NiO and $Ni(OH)_2$, there were also 3−4 times 10-cycle CV pretreatment (denoted as "initial") and all conditions of CVs were the same as those of Ni−S catalysts. OER stability was checked by the chronopotentiometry method at 10 mA cm^{-2}. The LSV curves were recorded before and after 40 and 65 h stability tests at 5 mV s^{-1}.

4.6. Single-Cell Configuration. Commercial Ni/NiO and the prepared NiS_2/Ni_3S_4 were used as anodic catalysts coated on the Ni fiber (area: 5 cm^2, thickness: 500 μm) with the mass loading of 5 mg cm^{-2}, while Pt (wt 60%)/C was used as the cathodic catalyst coated on carbon paper (area: 5 cm^2, thickness: 300 μm) with a mass loading of 0.8 mg cm^{-2}. The catalyst-coated substrate (CCS) structure was achieved by the Sono-Tek ultrasonic spraying system. FAA-3-SOLUT-10 and AP1-HNN8−00-X were used as the ionomers in the corresponding FAA-3-50 and AF1-HNN8-50-based cells, which accounted for 20 wt % in NiS_2/Ni_3S_4 and 25 wt % in Pt/C inks. Two liters of 1 M KOH without further purification was used as the electrolyte and would be automatically compensated with D.I. water by a water-level sensor to keep the alkali concentration stable during continuous water electrolysis. FAA-3-50 and AF1-HNN8-50 membranes were used as the ionic conductors, which were immersed in 1 M KOH for 12 h before use. All of the tests were conducted at 60 ± 1 °C with an electrolyte feeding rate of 50 mL min^{-1}. To ensure repeatability, parallel cells were tested simultaneously and the torque used for assembling the cell was first fixed at 5.0 N·m and then at 10.0 N·m.

4.7. Single-Cell Testing Protocol. Single-cell measurements were performed with a potentiostat/galvanostatic setup (BioLogic, BCS-815). The protocol of single-cell testing is illustrated in Figure S15. First, it took 2 h to stabilize the temperature and flow rate of the electrolyte to 60 ± 1 °C and 50 mL min^{-1}, respectively. Second, sulfur leaching (10 CV cycles between 1.2 and 2.0 V, @100 mV s^{-1}), EIS (@200 mA cm^{-2}, from 10 kHz to 0.1 Hz, with an amplitude of 10 mA), and LSV (between 1.2 and 2.0 V, @5 mV s^{-1}) were performed three times for ∼0.5 h, followed by 0.5 h open-circuit voltage (OCV) and 6 h of conditioning at 1.7 V. Then, polarization curves were recorded by a galvanostatic method (@5 min $step^{-1}$, totally ∼2 h). After that, stability tests were launched at 1000 mA cm^{-2} for 500 h. Finally, the cells were disassembled and reassembled with a new pretreated AF1-HNN8-50 membrane and restarted with polarization curves.

■ ASSOCIATED CONTENT

Supporting Information

The Supporting Information is available free of charge at https://pubs.acs.org/doi/10.1021/acsami.2c01302.

Illustration of Ni−S-2 h, Ni−S-4 h, Ni−S-6 h, and chemical reactions during hydrothermal processes; LSV curves of Ni−S-2 h and Ni−S-6 h before and after sulfur leaching; Tafel slopes of Ni−S-2 h, Ni−S-6 h, and NiS_2/Ni_3S_4 before and after 40 and 65 h; TEM and HRTEM images of Ni−S-2 h and Ni−S-6 h; FTIR spectra of initial NiS_2/Ni_3S_4 and after 6 h half-cell water electrolysis at 1.35 and 1.7 V; precipitates prepared by $BaCl_2$ and anions in the electrolyte and the corresponding FTIR curve; HAADF images and corresponding elemental mapping of Ni and S after sulfur leaching and after 10 000 CVs; XRD pattern of Ni−S-2 h, Ni−S-6 h, and NiS_2/Ni_3S_4@carbon paper after sulfur leaching, 3000 and 10 000 CVs; double-layer capacitance measurements for determining the electrochemically active surface area for commercial Ni/NiO, $Ni(OH)_2$, and NiS_2/Ni_3S_4 before and after sulfur leaching; EIS of NiS_2/Ni_3S_4 before and after sulfur leaching, commercial Ni/NiO, and $Ni(OH)_2$; comparison of LSV curves of NiS_2/Ni_3S_4 in 1 M KOH and 1 M NaOH before and after sulfur leaching; photos of Ni/NiO and NiS_2/Ni_3S_4-based cells and single-cell protocol; EIS of NiS_2/Ni_3S_4 before and after sulfur leaching and initial Ni/NiO-based cells at 200 mA cm^{-2}; polarization curves of the NiS_2/Ni_3S_4-based cell after the 3rd sulfur leaching and 6 h conditioning; theoretical and practical volume of O_2 with time at 1000 mA cm^{-2} before and after 6 h@1.7 V and corresponding faradic efficiency; stability comparison of NiS_2/Ni_3S_4 with the literature; degradation of polarization curves for NiS_2/Ni_3S_4 and NiNiO-based cells during 500 and 50 h, and corresponding EIS curves; photos of key materials after 500 h, and EIS of NiS_2/Ni_3S_4-based cells before and after membrane refreshing; SEM images of NiS_2/Ni_3S_4@Ni fiber before and after 500 h; polarization performance comparison among FAA-3-X-based cells, and stability comparison among none-FAA-3-X-based cells (PDF)

■ AUTHOR INFORMATION

Corresponding Author

Meital Shviro − *Institute of Energy and Climate Research, Electrochemical Process Engineering (IEK-14), Forschungszentrum Jülich GmbH, 52425 Jülich, Germany;* orcid.org/0000-0002-9494-0233; Email: m.shviro@fz-juelich.de

Authors

Lu Xia − *Institute of Energy and Climate Research, Electrochemical Process Engineering (IEK-14), Forschungszentrum Jülich GmbH, 52425 Jülich, Germany; Faculty of Mechanical Engineering, RWTH Aachen University, 52062 Aachen, Germany*

Wulyu Jiang − *Institute of Energy and Climate Research, Electrochemical Process Engineering (IEK-14), Forschungszentrum Jülich GmbH, 52425 Jülich, Germany; Faculty of Mechanical Engineering, RWTH Aachen University, 52062 Aachen, Germany*

Heinrich Hartmann − *Central Institute for Engineering, Electronics and Analytics (ZEA-3), Forschungszentrum Jülich GmbH, 52425 Jülich, Germany*

Joachim Mayer − *ER-C 2, Forschungszentrum Jülich GmbH, 52425 Jülich, Germany; GFE, RWTH Aachen University, 52074 Aachen, Germany*

Werner Lehnert − *Institute of Energy and Climate Research, Electrochemical Process Engineering (IEK-14), Forschungszentrum Jülich GmbH, 52425 Jülich, Germany; Faculty of Mechanical Engineering, RWTH Aachen University, 52062 Aachen, Germany*

Complete contact information is available at: https://pubs.acs.org/10.1021/acsami.2c01302

Notes

The authors declare no competing financial interest.

■ ACKNOWLEDGMENTS

The authors acknowledge experimental support from Denise Beate Günther and Birgit Schumacher.

■ REFERENCES

(1) Buttler, A.; Spliethoff, H. Current Status of Water Electrolysis for Energy Storage, Grid Balancing and Sector Coupling via Power-to-Gas and Power-to-Liquids: a Review. *Renewable Sustainable Energy Rev.* **2018**, *82*, 2440−2454.

(2) Carmo, M.; Fritz, D. L.; Mergel, J.; Stolten, D. A Comprehensive Review on PEM Water Electrolysis. *Int. J. Hydrogen Energy* **2013**, *38*, 4901−4934.
(3) Ju, H.; Badwal, S.; Giddey, S. A Comprehensive Review of Carbon and Hydrocarbon Assisted Water Electrolysis for Hydrogen Production. *Appl. Energy* **2018**, *231*, 502−533.
(4) Lindquist, G. A.; Xu, Q.; Oener, S. Z.; Boettcher, S. W. Membrane Electrolyzers for Impure-Water Splitting. *Joule* **2020**, *4*, 2549−2561.
(5) Wang, M.; Wang, Z.; Gong, X.; Guo, Z. The Intensification Technologies to Water Electrolysis for Hydrogen Production – a Review. *Renewable Sustainable Energy Rev.* **2014**, *29*, 573−588.
(6) Miller, H. A.; Bouzek, K.; Hnat, J.; Loos, S.; Bernäcker, C. I.; Weißgärber, T.; Röntzsch, L.; Meier-Haack, J. Green Hydrogen from Anion Exchange Membrane Water Electrolysis: a Review of Recent Developments in Critical Materials and Operating Conditions. *Sustainable Energy Fuels* **2020**, *4*, 2114−2133.
(7) Gernaat, D. E. H. J.; de Boer, H. S.; Daioglou, V.; Yalew, S. G.; Müller, C.; an Vuuren, D. P. Climate Change Impacts on Renewable Energy Supply. *Nat. Clim. Change* **2021**, *11*, 119−125.
(8) Liu, C.; Shviro, M.; Gago, A. S.; Zaccarine, S. F.; Bender, G.; Gazdzicki, P.; Morawietz, T.; Biswas, I.; Rasinski, M.; Everwand, A.; Schierholz, R.; Pfeilsticker, J.; Müller, M.; Lopes, P. P.; Eichel, R. A.; Pivovar, B.; Pylypenko, S.; Friedrich, K. A.; Lehnert, W.; Carmo, M. Exploring the Interface of Skin-Layered Titanium Fibers for Electrochemical Water Splitting. *Adv. Energy Mater.* **2021**, *11*, No. 2002926.
(9) Liu, C.; Wippermann, K.; Rasinski, M.; Suo, Y.; Shviro, M.; Carmo, M.; Lehnert, W. Constructing a Multifunctional Interface Between Membrane and Porous Transport Layer for Water Electrolyzers. *ACS Appl. Mater. Interfaces* **2021**, *13*, 16182−16196.
(10) Park, S.; Shviro, M.; Hartmann, H.; Besmehn, A.; Mayer, J.; Stolten, D.; Carmo, M. Nickel Structures as a Template Strategy to Create Shaped Iridium Electrocatalysts for Electrochemical Water Splitting. *ACS Appl. Mater. Interfaces* **2021**, *13*, 13576−13585.
(11) Liu, C.; Carmo, M.; Bender, G.; Everwand, A.; Lickert, T.; Young, J. L.; Smolinka, T.; Stolten, D.; Lehnert, W. Performance Enhancement of PEM Electrolyzers through Iridium-Coated Titanium Porous Transport Layers. *Electrochem. Commun.* **2018**, *97*, 96−99.
(12) Arges, C. G.; Zhang, L. Anion Exchange Membranes' Evolution toward High Hydroxide Ion Conductivity and Alkaline Resiliency. *ACS Appl. Energy Mater.* **2018**, *1*, 2991−3012.
(13) Cao, Y.-C.; Wu, X.; Scott, K. A Quaternary Ammonium Grafted Poly Vinyl Benzyl Chloride Membrane for Alkaline Anion Exchange Membrane Water Electrolysers with No-Noble-Metal Catalysts. *Int. J. Hydrogen Energy* **2012**, *37*, 9524−9528.
(14) Chu, X.; Shi, Y.; Liu, L.; Huang, Y.; Li, N. Piperidinium-Functionalized Anion Exchange Membranes and Their Application in Alkaline Fuel Cells and Water Electrolysis. *J. Mater. Chem. A* **2019**, *7*, 7717−7727.
(15) Fortin, P.; Khoza, T.; Cao, X.; Martinsen, S. Y.; Oyarce Barnett, A.; Holdcroft, S. High-performance Alkaline Water Electrolysis Using Aemion Anion Exchange Membranes. *J. Power Sources* **2020**, *451*, No. 227814.
(16) Hagesteijn, K. F. L.; Jiang, S.; Ladewig, B. P. A Review of the Synthesis and Characterization of Anion Exchange Membranes. *J. Mater. Sci.* **2018**, *53*, 11131−11150.
(17) Chen, P.; Hu, X. High-Efficiency Anion Exchange Membrane Water Electrolysis Employing Non-Noble Metal Catalysts. *Adv. Energy Mater.* **2020**, *10*, No. 2002285.
(18) Cossar, E.; Oyarce Barnett, A.; Seland, F.; Baranova, E. A. The Performance of Nickel and Nickel-Iron Catalysts Evaluated as Anodes in Anion Exchange Membrane Water Electrolysis. *Catalysts* **2019**, *9*, No. 814.
(19) Henkensmeier, D.; Najibah, M.; Harms, C.; Žitka, J.; Hnát, J.; Bouzek, K. Overview: State-of-the-Art Commercial Membranes for Anion Exchange Membrane Water Electrolysis. *J. Electrochem. Energy Convers. Storage* **2021**, *18*, No. 024001.
(20) Jiao, S.; Fu, X.; Wang, S.; Zhao, Y. Perfecting the Electrocatalysts via Imperfections: towards Large-Scale Deployment of Water Electrolysis Technology. *Energy Environ. Sci.* **2021**, *14*, 1722−1770.
(21) Kwon, C. Y.; Jeong, J. Y.; Yang, J.; Park, Y. S.; Jeong, J.; Park, H.; Kim, Y.; Choi, S. M. Effect of Copper Cobalt Oxide Composition on Oxygen Evolution Electrocatalysts for Anion Exchange Membrane Water Electrolysis. *Front. Chem.* **2020**, *8*, No. 600908.
(22) Liao, H.; Guo, X.; Hou, Y.; Liang, H.; Zhou, Z.; Yang, H. Construction of Defect-Rich Ni-Fe-Doped $K_{0.23}MnO_2$ Cubic Nanoflowers via Etching Prussian Blue Analogue for Efficient Overall Water Splitting. *Small* **2020**, *16*, No. 1905223.
(23) Xi, W.; Yan, G.; Lang, Z.; Ma, Y.; Tan, H.; Zhu, H.; Wang, Y.; Li, Y. Oxygen-Doped Nickel Iron Phosphide Nanocube Arrays Grown on Ni Foam for Oxygen Evolution Electrocatalysis. *Small* **2018**, *14*, No. 1802204.
(24) Xuan, C.; Zhang, J.; Wang, J.; Wang, D. Rational Design and Engineering of Nanomaterials Derived from Prussian Blue and Its Analogs for Electrochemical Water Splitting. *Chem. − Asian J.* **2020**, *15*, 958−972.
(25) Zhao, D.; Lu, Y.; Ma, D. Effects of Structure and Constituent of Prussian Blue Analogs on Their Application in Oxygen Evolution Reaction. *Molecules* **2020**, *25*, No. 2304.
(26) Cao, L. M.; Hu, Y. W.; Tang, S. F.; Iljin, A.; Wang, J. W.; Zhang, Z. M.; Lu, T. B. Fe-CoP Electrocatalyst Derived from a Bimetallic Prussian Blue Analogue for Large-Current-Density Oxygen Evolution and Overall Water Splitting. *Adv. Sci.* **2018**, *5*, No. 1800949.
(27) Cui, Y.; Xue, Y.; Zhang, R.; Zhang, J.; Li, X.; Zhu, X. Vanadium-Cobalt Oxyhydroxide Shows Ultralow Overpotential for the Oxygen Evolution Reaction. *J. Mater. Chem. A* **2019**, *7*, 21911−21917.
(28) Jiang, M.; Li, Y.; Lu, Z.; Sun, X.; Duan, X. Binary Nickel-Iron Nitride Nanoarrays as Bifunctional Electrocatalysts for Overall Water Splitting. *Inorg. Chem. Front.* **2016**, *3*, 630−634.
(29) Li, P.; Duan, X.; Kuang, Y.; Li, Y.; Zhang, G.; Liu, W.; Sun, X. Tuning Electronic Structure of NiFe Layered Double Hydroxides with Vanadium Doping toward High Efficient Electrocatalytic Water Oxidation. *Adv. Energy Mater.* **2018**, *8*, No. 1703341.
(30) Wang, D.; Li, Q.; Han, C.; Lu, Q.; Xing, Z.; Yang, X. Atomic and Electronic Modulation of Self-Supported Nickel-Vanadium Layered Double Hydroxide to Accelerate Water Splitting Kinetics. *Nat. Commun.* **2019**, *10*, No. 3899.
(31) Xuan, C.; Peng, Z.; Xia, K.; Wang, J.; Xiao, W.; Lei, W.; Gong, M.; Huang, T.; Wang, D. Self-Supported Ternary Ni-Fe-P Nanosheets Derived from Metal-Organic Frameworks as Efficient Overall Water Splitting Electrocatalysts. *Electrochim. Acta* **2017**, *258*, 423−432.
(32) Zhang, B.; Xiao, C.; Xie, S.; Liang, J.; Chen, X.; Tang, Y. Iron-Nickel Nitride Nanostructures in Situ Grown on Surface-Redox-Etching Nickel Foam: Efficient and Ultrasustainable Electrocatalysts for Overall Water Splitting. *Chem. Mater.* **2016**, *28*, 6934−6941.
(33) Yu, F.; Zhou, H.; Huang, Y.; Sun, J.; Qin, F.; Bao, J.; Goddard, W. A., 3rd; Chen, S.; Ren, Z. High-Performance Bifunctional Porous Non-Noble Metal Phosphide Catalyst for Overall Water Splitting. *Nat. Commun.* **2018**, *9*, No. 2551.
(34) Thangavel, P.; Ha, M.; Kumaraguru, S.; Meena, A.; Singh, A. N.; Harzandi, A. M.; Kim, K. S. Graphene-Nanoplatelets-Supported NiFe-MOF: High-Efficiency and Ultra-Stable Oxygen Electrodes for Sustained Alkaline Anion Exchange Membrane Water Electrolysis. *Energy Environ. Sci.* **2020**, *13*, 3447−3458.
(35) Harzandi, A. M.; Shadman, S.; Nissimagoudar, A. S.; Kim, D. Y.; Lim, H. D.; Lee, J. H.; Kim, M. G.; Jeong, H. Y.; Kim, Y.; Kim, K. S. Ruthenium Core-Shell Engineering with Nickel Single Atoms for Selective Oxygen Evolution via Nondestructive Mechanism. *Adv. Energy Mater.* **2021**, *11*, No. 2003448.
(36) Meena, A.; Thangavel, P.; Jeong, D. S.; Singh, A. N.; Jana, A.; Im, H.; Nguyen, D. A.; Kim, K. S. Crystalline-Amorphous Interface of Mesoporous Ni_2P@$FePO_xH_y$ for Oxygen Evolution at High Current Density in Alkaline-Anion-Exchange-Membrane Water-Electrolyzer. *Appl. Catal., B* **2022**, *306*, No. 121127.

(37) Thangavel, P.; Kim, G.; Kim, K. S. Electrochemical Integration of Amorphous NiFe (Oxy)Hydroxides on Surface-Activated Carbon Fibers for High-Efficiency Oxygen Evolution in Alkaline Anion Exchange Membrane Water Electrolysis. *J. Mater. Chem. A* **2021**, *9*, 14043−14051.
(38) Zhou, W.; Wu, X.-J.; Cao, X.; Huang, X.; Tan, C.; Tian, J.; Liu, H.; Wang, J.; Zhang, H. Ni_3S_2 Nanorods/Ni Foam Composite Electrode with Low Overpotential for Electrocatalytic Oxygen Evolution. *Energy Environ. Sci.* **2013**, *6*, 2921−2924.
(39) Shang, X.; Li, X.; Hu, W.-H.; Dong, B.; Liu, Y.-R.; Han, G.-Q.; Chai, Y.-M.; Liu, Y.-Q.; Liu, C.-G. In Situ Growth of Ni_xS_y Controlled by Surface Treatment of Nickel Foam as Efficient Electrocatalyst for Oxygen Evolution Reaction. *Appl. Surf. Sci.* **2016**, *378*, 15−21.
(40) Zhang, W.; Song, H.; Cheng, Y.; Liu, C.; Wang, C.; Khan, M. A. N.; Zhang, H.; Liu, J.; Yu, C.; Wang, L.; Li, J. Core-Shell Prussian Blue Analogs with Compositional Heterogeneity and Open Cages for Oxygen Evolution Reaction. *Adv. Sci.* **2019**, *6*, No. 1801901.
(41) Pavel, C. C.; Cecconi, F.; Emiliani, C.; Santiccioli, S.; Scaffidi, A.; Catanorchi, S.; Comotti, M. Highly Efficient Platinum Group Metal Free Based Membrane-Electrode Assembly for Anion Exchange Membrane Water Electrolysis. *Angew. Chem., Int. Ed.* **2014**, *53*, 1378−1381.
(42) Wang, L.; Weissbach, T.; Reissner, R.; Ansar, A.; Gago, A. S.; Holdcroft, S.; Friedrich, K. A. High Performance Anion Exchange Membrane Electrolysis Using Plasma-Sprayed, Non-Precious-Metal Electrodes. *ACS Appl. Energy Mater.* **2019**, *2*, 7903−7912.
(43) Xuan, C.; Lei, W.; Wang, J.; Zhao, T.; Lai, C.; Zhu, Y.; Sun, Y.; Wang, D. Sea Urchin-Like Ni-Fe Sulfide Architectures as Efficient Electrocatalysts for the Oxygen Evolution Reaction. *J. Mater. Chem. A* **2019**, *7*, 12350−12357.
(44) Wu, Q.; Xiao, M.; Wang, W.; Cui, C. In Situ Coordination Environment Tuning of Cobalt Sites for Efficient Water Oxidation. *ACS Catal.* **2019**, *9*, 11734−11742.
(45) Mabayoje, O.; Shoola, A.; Wygant, B. R.; Mullins, C. B. The Role of Anions in Metal Chalcogenide Oxygen Evolution Catalysis: Electrodeposited Thin Films of Nickel Sulfide as "Pre-Catalysts. *ACS Energy Lett.* **2016**, *1*, 195−201.
(46) Jin, S. Are Metal Chalcogenides, Nitrides, and Phosphides Oxygen Evolution Catalysts or Bifunctional Catalysts? *ACS Energy Lett.* **2017**, *2*, 1937−1938.
(47) Lee, M.; Oh, H.-S.; Cho, M. K.; Ahn, J.-P.; Hwang, Y. J.; Min, B. K. Activation of a Ni Electrocatalyst through Spontaneous Transformation of Nickel Sulfide to Nickel Hydroxide in an Oxygen Evolution Reaction. *Appl. Catal., B* **2018**, *233*, 130−135.
(48) Li, W.; Xiong, D.; Gao, X.; Liu, L. The Oxygen Evolution Reaction Enabled by Transition Metal Phosphide and Chalcogenide Pre-Catalysts with Dynamic Changes. *Chem. Commun.* **2019**, *55*, 8744−8763.
(49) Fan, K.; Zou, H.; Lu, Y.; Chen, H.; Li, F.; Liu, J.; Sun, L.; Tong, L.; Toney, M. F.; Sui, M.; Yu, J. Direct Observation of Structural Evolution of Metal Chalcogenide in Electrocatalytic Water Oxidation. *ACS Nano* **2018**, *12*, 12369−12379.
(50) Zhao, G.; Zhang, Y.; Yang, L.; Jiang, Y.; Zhang, Y.; Hong, W.; Tian, Y.; Zhao, H.; Hu, J.; Zhou, L.; Hou, H.; Ji, X.; Mai, L. Nickel Chelate Derived NiS_2 Decorated with Bifunctional Carbon: An Efficient Strategy to Promote Sodium Storage Performance. *Adv. Funct. Mater.* **2018**, *28*, No. 1803690.
(51) Zeng, L.; Liu, Z.; Sun, K.; Chen, Y.; Zhao, J.; Chen, Y.; Pan, Y.; Lu, Y.; Liu, Y.; Liu, C. Multiple Modulations of Pyrite Nickel Sulfides via Metal Heteroatom Doping Engineering for Boosting Alkaline and Neutral Hydrogen Evolution. *J. Mater. Chem. A* **2019**, *7*, 25628−25640.
(52) Nesbitt, H.; Legrand, D.; Bancroft, G. Interpretation of Ni2p XPS Spectra of Ni Conductors and Ni Insulators. *Phys. Chem. Miner.* **2000**, *27*, 357−366.
(53) Huang, S.; Li, Y.; Chen, S.; Wang, Y.; Wang, Z.; Fan, S.; Zhang, D.; Yang, H. Y. Regulating the Breathing of Mesoporous $Fe_{0.95}S_{1.05}$ Nanorods for Fast and Durable Sodium Storage. *Energy Storage Mater.* **2020**, *32*, 151−158.
(54) Wang, L.; Zhu, Y.; Li, H.; Li, Q.; Qian, Y. Hydrothermal Synthesis of NiS Nanobelts and NiS_2 Microspheres Constructed of Cuboids Architectures. *J. Solid State Chem.* **2010**, *183*, 223−227.
(55) Wan, K.; Luo, J.; Zhou, C.; Zhang, T.; Arbiol, J.; Lu, X.; Mao, B. W.; Zhang, X.; Fransaer, J. Hierarchical Porous Ni_3S_4 with Enriched High-Valence Ni Sites as a Robust Electrocatalyst for Efficient Oxygen Evolution Reaction. *Adv. Funct. Mater.* **2019**, *29*, No. 1900315.
(56) He, Y.; Zhang, X.; Wang, S.; Meng, J.; Sui, Y.; Wei, F.; Qi, J.; Meng, Q.; Ren, Y.; Zhuang, D. Rubik's Cube-Like Ni_3S_4/CuS_2 Nanocomposite for High-Performance Supercapacitors. *J. Alloys Compd.* **2020**, *847*, No. 156312.
(57) Nandhini, S.; et al. Facile Microwave-Hydrothermal Synthesis of NiS Nanostructures for Supercapacitor Applications. *Appl. Surf. Sci.* **2018**, *449*, 485−491.
(58) Wang, H.-Y.; Hsu, Y.-Y.; Chen, R.; Chan, T.-S.; Chen, H. M.; Liu, B. Ni^{3+}-Induced Formation of Active NiOOH on the Spinel Ni-Co Oxide Surface for Efficient Oxygen Evolution Reaction. *Adv. Energy Mater.* **2015**, *5*, No. 1500091.
(59) Tahir, M.; Pan, L.; Zhang, R.; Wang, Y.-C.; Shen, G.; Aslam, I.; Qadeer, M. A.; Mahmood, N.; Xu, W.; Wang, L.; Zhang, X.; Zou, J.-J. High-Valence-State NiO/Co_3O_4 Nanoparticles on Nitrogen-Doped Carbon for Oxygen Evolution at Low Overpotential. *ACS Energy Lett.* **2017**, *2*, 2177−2182.
(60) Ma, Q.; Hu, C.; Liu, K.; Hung, S.-F.; Ou, D.; Chen, H. M.; Fu, G.; Zheng, N. Identifying the Electrocatalytic Sites of Nickel Disulfide in Alkaline Hydrogen Evolution Reaction. *Nano Energy* **2017**, *41*, 148−153.
(61) Kamyshny, A.; Jenny, G.; Dan, R.; Ovadia, L.; et al. Equilibrium Distribution of Polysulfide Ions in Aqueous Solutions at 25°C: a New Approach for the Study of Polysulfides' Equilibria. *Environ. Sci. Technol.* **2004**, *38*, 6633−6644.
(62) Wang, R.; Xu, C.; Lee, J.-M. High Performance Asymmetric Supercapacitors: New NiOOH Nanosheet/Graphene Hydrogels and Pure Graphene Hydrogels. *Nano Energy* **2016**, *19*, 210−221.
(63) Xiao, M.; Tian, Y.; Yan, Y.; Feng, K.; Miao, Y. Electrodeposition of $Ni(OH)_2$/NiOOH in the Presence of Urea for the Improved Oxygen Evolution. *Electrochim. Acta* **2015**, *164*, 196−202.
(64) Zhang, Y.; Sun, W.; Rui, X.; Li, B.; Tan, H. T.; Guo, G.; Madhavi, S.; Zong, Y.; Yan, Q. One-Pot Synthesis of Tunable Crystalline Ni_3S_4@Amorphous MoS_2 Core/Shell Nanospheres for High-Performance Supercapacitors. *Small* **2015**, *11*, 3694−3702.
(65) Kaspar, J.; Bazarjani, M. S.; Schitco, C.; Gurlo, A.; Graczyk-Zajac, M.; Riedel, R. Electrochemical Study of NiO Nanosheets: toward the Understanding of Capacity Fading. *J. Mater. Sci.* **2017**, *52*, 6498−6505.
(66) Yavuz, A.; Ozdemir, N.; Erdogan, P. Y.; Zengin, H.; Zengin, G.; Bedir, M. Nickel-Based Materials Electrodeposited from a Deep Eutectic Solvent on Steel for Energy Storage Devices. *Appl. Phys. A* **2019**, *125*, No. 494.
(67) Sivakumar, S.; Soundhirarajan, P.; Venkatesan, A.; Khatiwada, C. P. Spectroscopic Studies and Antibacterial Activities of Pure and Various Levels of Cu-Doped $BaSO_4$ Nanoparticles. *Spectrochim. Acta, Part A* **2015**, *151*, 895−907.
(68) Chen, W.; Wang, H.; Li, Y.; Liu, Y.; Sun, J.; Lee, S.; Lee, J. S.; Cui, Y. In Situ Electrochemical Oxidation Tuning of Transition Metal Disulfides to Oxides for Enhanced Water Oxidation. *ACS Cent. Sci.* **2015**, *1*, 244−251.
(69) Xu, X.; Song, F.; Hu, X. A Nickel Iron Diselenide-Derived Efficient Oxygen-Evolution Catalyst. *Nat. Commun.* **2016**, *7*, No. 12324.
(70) Ni, B.; He, T.; Wang, J. O.; Zhang, S.; Ouyang, C.; Long, Y.; Zhuang, J.; Wang, X. The Formation of $(NiFe)S_2$ Pyrite Mesocrystals as Efficient Pre-catalysts for Water Oxidation. *Chem. Sci.* **2018**, *9*, 2762−2767.
(71) Michael, J. D.; Demeter, E. L.; Illes, S. M.; Fan, Q.; Boes, J. R.; Kitchin, J. R. Alkaline Electrolyte and Fe Impurity Effects on the Performance and Active-Phase Structure of NiOOH Thin Films for

https://doi.org/10.1021/acsami.2c01302
ACS Appl. Mater. Interfaces 2022, 14, 19397−19408

OER Catalysis Applications. *J. Phys. Chem. C* **2015**, *119*, 11475−11481.
(72) Klaus, S.; Cai, Y.; Louie, M. W.; Trotochaud, L.; Bell, A. T. Effects of Fe Electrolyte Impurities on $Ni(OH)_2$/NiOOH Structure and Oxygen Evolution Activity. *J. Phys. Chem. C* **2015**, *119*, 7243−7254.
(73) Gocyla, M.; Kuehl, S.; Shviro, M.; Heyen, H.; Selve, S.; Dunin-Borkowski, R. E.; Heggen, M.; Strasser, P. Shape Stability of Octahedral PtNi Nanocatalysts for Electrochemical Oxygen Reduction Reaction Studied by In Situ Transmission Electron Microscopy. *ACS Nano* **2018**, *12*, 5306−5311.
(74) Shviro, M.; Gocyla, M.; Schierholz, R.; Tempel, H.; Kungl, H.; Eichel, R. A.; Dunin-Borkowski, R. E. Transformation of Carbon-Supported Pt-Ni Octahedral Electrocatalysts into Cubes: toward Stable Electrocatalysis. *Nanoscale* **2018**, *10*, 21353−21362.
(75) Meena, A.; Thangavel, P.; Nissimagoudar, A. S.; Narayan Singh, A.; Jana, A.; Sol Jeong, D.; Im, H.; Kim, K. S. Bifunctional Oxovanadate Doped Cobalt Carbonate for High-Efficient Overall Water Splitting in Alkaline-Anion-Exchange-Membrane Water-Electrolyzer. *Chem. Eng. J.* **2022**, *430*, No. 132623.

https://doi.org/10.1021/acsami.2c01302
ACS Appl. Mater. Interfaces 2022, 14, 19397−19408